1

Measurement and control of quantum cavities with electronic atoms

A. N. Cleland

1.1 Introduction

This chapter describes a method to control and measure quantum cavities, achieved using a superconducting phase qubit, a type of electronic atom. The phase qubit has been under intensive development for use as a quantum processing element in a quantum computer. We have recently used it to demonstrate the quantum control and measurement of excitations in resonant cavities, including controlling photons in superconducting microwave resonators (Hofheinz *et al.*, 2008; Wang *et al.*, 2008; Hofheinz *et al.*, 2009; Wang *et al.*, 2009*a*; Mariantoni *et al.*, 2011; Wang *et al.*, 2011), as well as phonons in microwave-frequency mechanical resonators (OConnell *et al.*, 2010). The discussion here focusses on the quantum control of electromagnetic resonators; we refer the interested reader to other recently-published references for further information on quantum control of mechanical resonators (Marquardt *et al.*, 2011; OConnell *et al.*, 2010).

The phase qubit is a particular implementation of the Josephson junction. I begin by describing the physics of the Josephson junction, and how the junction is embedded in an electrical circuit to provide the critical nonlinearity needed for quantum circuit operation. We have used this electrical circuit as a quantum two-level system, the prototypical qubit, and as a three-level system, where it can be called a "qutrit". I then describe how we have used the phase qubit in conjunction with highly linear microwave resonators to perform a number of interesting experiments, including the on-demand creation and storage of photon Fock states, and the synthesis of arbitrary superpositions of Fock states. I also briefly summarize more recent results, including entangling photons stored in two physically separate microwave resonators, as well as playing a "shell game" with the photons stored in three microwave resonators.

1.2 A Josephson junction as a tunable two-level system

The Josephson junction is the simplest active device found in superconducting circuitry. A Josephson junction is formed when a superconducting metal is interrupted by a weak link that impedes the flow of electrons. A straightforward and robust type

of Josephson junction is formed by separating two superconducting metal electrodes by a thin insulating barrier, through which electrons (in the form of Cooper pairs) can tunnel, as shown in Fig. 1.1. This device is known as a superconductor-insulator-superconductor (SIS) tunnel junction, and can be fabricated reliably and controllably, with a wide range of operating parameters, using thin-film lithographic techniques. The ease of fabrication, stability, adaptability and compatibility with complex circuit layouts have ensured that this type of Josephson junction is by far the most commonly used. There are other types of Josephson junctions that can be created using other types of weak links, but all share the same basic physics; more information can be found in Barone and Paterno 1982 and Tinkham 2004.

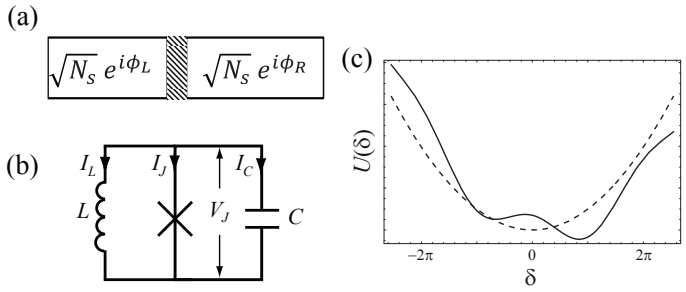

Fig. 1.1 (a) A superconductor-insulator-superconductor Josephson junction, with two superconducting electrodes separated by a thin insulating barrier (hashed area). Each superconducting electrode can be represented by a macroscopic wavefunction, here shown with Cooper pair density N_s and phases $\phi_{L,R}$ for the left and right electrodes. (b) Equivalent electrical circuit for the phase qubit. The Josephson junction is represented by a cross, and is in parallel with a capacitor $C = C_J + C_e$, the parallel combination of an external capacitor and the junction capacitance, and an external inductor L. (c) Potential energy $U(\delta)$ for the phase qubit (solid line), showing a small local minimum on the left, and an absolute minimum on the right. The overall parabolic dependence (dashed line) is due to the flux energy stored in the inductor L.

The Josephson junction was discovered in 1962 (Josephson, 1962). Its electrical behavior is dominated by the dynamics of the macroscopic Ginzburg-Landau wavefunctions that describe the Bose-condensed Cooper pairs on either side of the junction. The behavior is dominated by the difference $\delta = \phi_L - \phi_R$ of the phases of the wavefunctions on the left and right sides of the junction. Remarkably, two conventional circuit parameters, the current I_J through the junction, and the voltage V_J across the junction, are directly controlled by this phase difference, as described by the dc and ac Josephson relations . The dc Josephson relation gives the value of the supercurrent through the junction, which flows even in the absence of an applied voltage:

$$I_J = I_0 \sin(\delta), \tag{1.1}$$

where I_0 is the junction's critical current, determined by the area and thickness of the insulating barrier. With a voltage V_J applied across the junction, the ac Josephson

relation states that the phase evolves according to

$$\frac{d\delta}{dt} = \frac{2e}{\hbar} V_J. \tag{1.2}$$

Combining these relations shows that a voltage-biased Josephson junction will have a supercurrent that oscillates in time at the Josephson frequency $2eV_J/h$. This relation has been tested experimentally and shown to be extremely accurate. The simple relation between frequency and voltage is the basis of the Josephson voltage standard, where a precise microwave frequency applied to a large number of series-connected Josephson junctions results in a very precise voltage (see e.g. Benz and Hamilton 1996).

Josephson junctions have been incorporated in a wide array of superconducting quantum circuits (Caldeira and Legget, 1981; Devoret *et al.*, 1985; Leggett *et al.*, 1987; Clarke *et al.*, 1988; Mooij *et al.*, 1999; van der Wal *et al.*, 2000; **?**; Chiorescu *et al.*, 2003; Lehnert *et al.*, 2003; Pashkin *et al.*, 2003; Yamamoto *et al.*, 2003; Chiorescu *et al.*, 2004; Cooper *et al.*, 2004; Simmonds *et al.*, 2004; Wallraff *et al.*, 2004). The phase qubit provides one particular implementation, as shown in Fig. 1.1, comprising a Josephson junction, indicated by a cross, in parallel with a capacitor C and an inductor L. The capacitance C is provided by the capacitance C_J of the Josephson junction itself, and by an external capacitor C_e included in the design of the circuit. The parallel combination yields a total capacitance $C = C_J + C_e$. This capacitor supports the standard displacement current $I_C = CdV_J/dt$.

The circuit dynamics can be understood using standard circuit theory. If there is a voltage V_J across the circuit, the current through the inductor is

$$I_L = \frac{1}{L}\int V_J(t')dt' = \frac{1}{L}\frac{\hbar}{2e}\delta - I, \tag{1.3}$$

where $-I$ is an integration constant, set experimentally by an external flux coil magnetically coupled to the inductance L; I is effectively the bias current of the Josephson junction, as will be clear. The inductor current is equal and opposite in sign to the current through the parallel combination of junction and capacitor:

$$-I_L = I_C + I_J = C\frac{dV_J}{dt} + I_J = \frac{\hbar}{2e}C\frac{d^2\delta}{dt^2} + I_0\sin(\delta). \tag{1.4}$$

These equations yield the equation of motion for the phase δ:

$$\left(\frac{\hbar}{2e}\right)^2 C\frac{d^2\delta}{dt^2} = -\frac{\partial}{\partial\delta}\left[\left(\frac{\hbar}{2e}\right)^2\frac{1}{2L}\delta^2 - \frac{\hbar}{2e}I\delta - \frac{\hbar}{2e}I_0\cos(\delta)\right] = -\frac{\partial U}{\partial\delta}. \tag{1.5}$$

This equation is identical to that of a one-dimensional classical particle with mass $(\hbar/2e)^2C$, moving in a potential $U(\delta)$ given by the expression in the square brackets. The equation of motion can be cast into the Lagrangian form, with the kinetic T and potential U energies given by

$$T = \frac{1}{2}\left(\frac{\hbar}{2e}\right)^2 C\left(\frac{d\delta}{dt}\right)^2 = \frac{\hbar^2}{4E_C}\dot{\delta}^2, \tag{1.6}$$

$$U(\delta) = \frac{1}{2L}\left(\frac{\hbar}{2e}\right)^2 \delta^2 - E_J(s\delta - \cos(\delta)), \tag{1.7}$$

where we define the charging energy $E_C = (2e)^2/2C$, the Josephson energy $E_J = \hbar I_0/2e$, and the bias parameter $s = I/I_0$. The form of the potential energy is shown in Fig. 1.1(c), with an overall parabolic shape with undulations from the Josephson term. For the parameters in the figure, which are typical for the phase qubit, the potential function displays two local minima spaced in δ by approximately 2π. The phase particle is typically trapped either in the absolute minimum on the right, or in the small local minimum on the left. When operated as a qubit, the phase particle is placed by a reset procedure in the left, local, minimum; the right side absolute minimum is used when measuring the qubit state (see below).

An important feature of the phase qubit is that its dynamics necessarily include dissipation, which causes energy relaxation. This implies that when the particle is trapped in a potential minimum, in the absence of spurious noise or external excitations it will relax to its minimum energy. The dissipation can be attributed in part to the non-zero coupling of the qubit circuit to the external electrical cabling used to measure and control the qubit. This cabling presents an impedance of order 50 Ω, but the coupling to the qubit is so weak that the dissipation due to this channel is well below the experimentally observed dissipation. The dominant dissipation is instead thought to be a combination of loss in spurious two-level systems (TLS) in the insulating materials included in the qubit fabrication, and possibly excess quasiparticles in the qubit's superconducting electrodes; however, a detailed understanding of the dominant dissipative mechanism is still being sought. The dissipation can be accounted for phenomenologically by adding a resistor R to the electrical circuit in Fig. 1.1b, in parallel with the capacitor C. In properly designed qubits, the amount of dissipation due to this resistance is small, with the effective quality factor of the equivalent circuit in the range of 10^4 to 10^5, so that the short-time dynamics are essentially unaffected by dissipation; we will return to this issue later.

We can find the Hamiltonian for the system in the usual way. We define the Lagrangian $\mathcal{L} = T - U$, then calculate the momentum conjugate to the coordinate δ (Goldstein *et al.*, 2002):

$$p = \frac{\partial \mathcal{L}}{\partial \dot{\delta}} = \left(\frac{\hbar}{2e}\right)^2 C\,\dot{\delta}. \tag{1.8}$$

The Hamiltonian is then

$$H = p\dot{\delta} - \mathcal{L} = \frac{1}{2}\left(\frac{2e}{\hbar}\right)^2 \frac{p^2}{C} + U(\delta). \tag{1.9}$$

The Hamiltonian can now be quantized in the usual way; this is perhaps surprising, as the Hamiltonian (1.9) is that for a classical electrical circuit, other than the presence of the Josephson element. However, there is no *a priori* reason that electrical circuits should not obey the quantum mechanical equations of motion, including ones for macroscopic variables such as current and voltage. We therefore introduce the quantum operators $\hat{\delta}$ and $\hat{p}$ and impose the usual commutation relation

$$[\hat{\delta}, \hat{p}] = i\hbar, \tag{1.10}$$

the analog of the position-momentum uncertainty for a particle. The coordinate representation of the momentum operator is then given by

$$\hat{p} \rightarrow -i\hbar \frac{\partial}{\partial \delta}, \tag{1.11}$$

which allows us to transform the classical Hamiltonian (1.9) to its quantum mechanical form,

$$\hat{H}_q = \frac{1}{2}\left(\frac{2e}{\hbar}\right)^2 \frac{\hat{p}^2}{C} + U(\hat{\delta}). \tag{1.12}$$

The time-dependent Schrödinger equation for the wavefunction $|\Psi\rangle$ that represents the state of the electrical circuit is then given by

$$\hat{H}_q |\Psi\rangle = i\hbar \frac{d|\Psi\rangle}{dt}. \tag{1.13}$$

It is often more convenient to write the quantum mechanical Hamiltonian (1.12) in its coordinate representation,

$$\hat{H}_q \rightarrow -\frac{1}{2}\frac{(2e)^2}{C}\frac{\partial^2}{\partial \delta^2} + U(\delta) = -E_C \frac{\partial^2}{\partial \delta^2} + U(\delta). \tag{1.14}$$

The Schrödinger equation in the coordinate representation is

$$-E_C \frac{\partial^2 \Psi}{\partial \delta^2} + U(\delta)\Psi = i\hbar \frac{\partial \Psi}{\partial t}. \tag{1.15}$$

The energy eigenstates, i.e. the stationary solutions to (1.15), include solutions that are localized in the left local minimum in Fig. 1.1. Although these energy eigenstates can be solved for directly, we instead use a harmonic approximation that captures the qualitative behavior in the local minimum, as illustrated in Fig. 1.2(a). Near the minimum, the potential $U(\delta)$ can be roughly approximated by that of a harmonic oscillator, i.e. the potential energy is approximately quadratic in the displacement from the minimum. The energy eigenstates are then approximately those of a harmonic oscillator, whose frequency is determined by the curvature $d^2U/d\delta^2$ at the minimum. This frequency is defined as the junction's plasma frequency ω_p (Geller and Cleland, 2005)

$$\omega_p \equiv \frac{\sqrt{2E_C E_J}}{\hbar}\left(1 - s^2\right)^{1/4}. \tag{1.16}$$

Note the dependence on the bias s, which reflects the tunability of the qubit frequency in this local minimum. The maximum value of the plasma frequency is at zero bias, $\omega_{p,max} = \sqrt{E_C E_J}$, which for the phase qubit is typically in the range of $\omega_{p,max}/2\pi \sim 10 - 20$ GHz.

In the harmonic approximation, the energy eigenstates in the local minimum are given by $(n + 1/2)\hbar\omega_p$, referenced to the local energy minimum. This is a reasonable

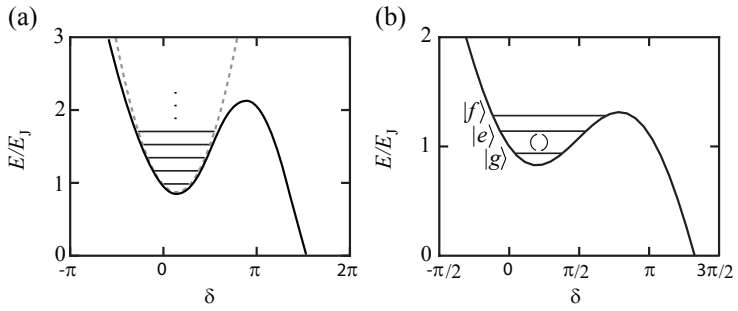

Fig. 1.2 Harmonic approximation and eigenstates of the Josephson potential. **a**, the dashed line overlay is a harmonic approximation to the actual potential, yielding evenly spaced energy levels. **b**, lowest energy levels of the left local minimum (other eigenstates not shown). The nonuniform spacing arises from the nonlinearity of the potential. The two lowest-lying levels of a local minimum, the ground state $|g\rangle$ and the first excited state $|e\rangle$, provide the qubit basis states.

approximation for a Josephson junction biased well below its critical current, $s \ll 1$ ($I \ll I_0$): All the energy levels are thus approximately evenly spaced by $\hbar\omega_p$. However, a harmonic oscillator is essentially impossible to use as a quantum bit; exciting a harmonic oscillator at its resonance frequency in a sense couples all of the energy levels together, so that controlling just two levels, which is needed for a qubit, is not possible. However, if a junction is biased very near its critical current, with s close to but somewhat less than 1, the plasma frequency is reduced in accordance with (1.16), but more importantly, the shape of the potential $U(\delta)$ becomes strongly anharmonic. This anharmonicity is so strong that the spacing between adjacent energy levels, even for the lowest levels, differs from that given by the harmonic approximation, as sketched in Fig. 1.2(b). The energy spacing between the lowest pair of levels, the ground state $|g\rangle$ and the first excited state $|e\rangle$, is slightly less than $\hbar\omega_p$, because these levels are not quite at the bottom of the potential. The spacing between the next higher pair of levels, the first excited state $|e\rangle$ and the next higher level, which we designate as $|f\rangle$, is in turn smaller than that of the first pair. This is quite remarkable: We have an electrical circuit in which a single quantum of energy changes the circuit response in a measurable way.

The phase qubit is typically operated so that the energy difference between the ground state $|g\rangle$ and the first excited state $|e\rangle$, $E_{eg} \equiv \hbar\omega_q$, is a few percent below $\hbar\omega_p$. The energy difference between the $|e\rangle$ and $|f\rangle$ states is then about 5% percent less than E_{eg}. This is sufficient so that one pair of these levels can be excited by appropriate choice of the frequency of an external microwave signal; this can be done with quite high precision (Lucero *et al.*, 2008). We typically use the ground state $|g\rangle$ and first excited state $|e\rangle$ as the qubit computational manifold. When instead used as a qutrit, the second excited level $|f\rangle$ is also involved; see Fig. 1.2.

We next turn to a quick review of the properties of quantum two-level systems.

1.2.1 Quantum two-level systems

A two-level system is the simplest non-trivial quantum system, occupying a two-dimensional Hilbert space. A two-level system is the fundamental computational element of a quantum computer, so the phrase "two-level system" and "quantum bit" are essentially interchangeable. The quantum mechanics of two-level systems is well developed and taught in most undergraduate courses in quantum mechanics; typically the formalism is developed in terms of the Pauli matrices, using which any manipulation of a two-level system can be performed. In the UC Santa Barbara phase qubit effort, we have chosen a non-standard convention for the basis vectors used to represent the different states; this chapter will adhere to that historical convention. We define the ground state $|g\rangle$ to have the basis vector in Hilbert space given by $|g\rangle = \begin{pmatrix} 1 \\ 0 \end{pmatrix}$, and for the excited state $|e\rangle = \begin{pmatrix} 0 \\ 1 \end{pmatrix}$ (this is reversed from the standard definition). The Hamiltonian can be written in this basis as

$$\hat{H}_q = \hbar\omega_q \begin{pmatrix} 0 & 0 \\ 0 & 1 \end{pmatrix}, \tag{1.17}$$

where the frequency ω_q is the frequency splitting between the ground and excited states, and we have set the ground state energy to zero. We use the standard Pauli matrices

$$\hat{\sigma}_x = \begin{pmatrix} 0 & 1 \\ 1 & 0 \end{pmatrix}, \hat{\sigma}_y = \begin{pmatrix} 0 & -i \\ i & 0 \end{pmatrix}, \hat{\sigma}_z = \begin{pmatrix} 1 & 0 \\ 0 & -1 \end{pmatrix}. \tag{1.18}$$

The Pauli raising $\hat{\sigma}_+$ and lowering $\hat{\sigma}_-$ matrices can be defined in terms of their action on the two energy eigenstates. We define $\hat{\sigma}_+ |g\rangle = |e\rangle$ and $\hat{\sigma}_- |e\rangle = |g\rangle$, so the matrix representations for these operators are

$$\hat{\sigma}_+ = \begin{pmatrix} 0 & 0 \\ 1 & 0 \end{pmatrix}, \text{ and } \hat{\sigma}_- = \begin{pmatrix} 0 & 1 \\ 0 & 0 \end{pmatrix}. \tag{1.19}$$

These can thus be written as $\hat{\sigma}_+ = \frac{1}{2}(\hat{\sigma}_x - i\,\hat{\sigma}_y)$ and $\hat{\sigma}_- = \frac{1}{2}(\hat{\sigma}_x + i\,\hat{\sigma}_y)$, again not the standard definitions. Using the raising and lowering operators, we can write the Hamiltonian more compactly as

$$\hat{H}_q = -\frac{1}{2}\hbar\omega_q(\hat{\sigma_z} - \hat{I}) = \hbar\omega_q\hat{\sigma}_+\,\hat{\sigma}_-. \tag{1.20}$$

Now, a classical bit in a classical computer has two values, 0 and 1, and the bit will always take on one or the other value. A quantum two-level system by contrast can be in a superposition of its two energy eigenstates $|g\rangle$ and $|e\rangle$, which are otherwise the equivalents of the classical 0 and 1 states respectively. With this special superposition allowed by quantum mechanics, a general quantum state $|\psi\rangle$ is of the form

$$|\psi\rangle = \alpha|g\rangle + \beta|e\rangle, \tag{1.21}$$

where α and β are complex-valued amplitudes for the two states. According to Born's rules for quantum state amplitudes, the probability of measuring the system in the

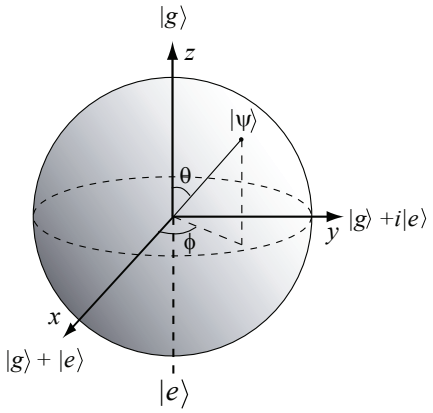

Fig. 1.3 The Bloch sphere.

ground state $|g\rangle$ is given by $P_g = |\alpha|^2$, while the probability for measuring it in the excited state $|e\rangle$ is $P_e = |\beta|^2$. Given that these are the only two possibilities, we have the probability closure rule $1 = P_g + P_e = |\alpha|^2 + |\beta|^2$. Hence we can always write $\alpha = e^{i\phi_g}\cos(\theta/2)$ and $\beta = e^{i\phi_e}\sin(\theta/2)$, with real values for the angles $\phi_{g,e}$ and θ. The probabilities are then given by $P_g = \cos^2(\theta/2)$ and $P_e = \sin^2(\theta/2)$. The overall complex phase of the state $|\psi\rangle$ is arbitrary (assuming this one quantum bit is our entire system), so we use the standard convention and set the phase for the $|g\rangle$ state to zero. With this simplification we can write the state as

$$|\psi\rangle = \cos(\theta/2)\,|g\rangle + e^{i\phi}\sin(\theta/2)\,|e\rangle, \tag{1.22}$$

where $\phi \equiv \phi_e - \phi_g$.

This designation puts the description of the two-level system into one-to-one correspondence with a geometric construction known as the Bloch sphere, as shown in Fig. 1.3; the spherical coordinates θ and ϕ are the usual polar and azimuthal angles, and the sphere has unit radius. In our convention, the "north pole" of the Bloch sphere is identified with the state $|g\rangle$, with angles $\theta = \phi = 0$, and the "south pole" is the state $|e\rangle$, with angles $\theta = \pi$ and $\phi = 0$. Points on the equator of the sphere, corresponding to the angle $\theta = \pi/2$, are equal-amplitude superpositions of $|g\rangle$ and $|e\rangle$, as shown in the figure; the x axis intersection with the sphere corresponds to $(|g\rangle + |e\rangle)/\sqrt{2}$, and the y axis corresponds to $(|g\rangle + i|e\rangle)/\sqrt{2}$.

Transformations of the quantum two-level state are in one-to-one correspondence with rotations on the Bloch sphere. Multiplication by the Pauli matrices $\hat{\sigma}_x$, $\hat{\sigma}_y$ and $\hat{\sigma}_z$ correspond to 90° rotations about the x, y and z axes, respectively; see Sakurai and Napolitano 2011. For example, a rotation of the Bloch sphere about the y axis by an angle φ is represented in Hilbert space by the corresponding transformation $R_y(\varphi) = \exp(-i(\varphi/2)\hat{\sigma}_y)$, where the usual polynomial expansion of the exponential is used to evaluate this expression. This can be written as

$$R_y(\varphi) = \hat{I}\cos(\varphi/2) - i\,\hat{\sigma}_y\sin(\varphi/2) = \begin{pmatrix} \cos(\varphi/2) & -\sin(\varphi/2) \\ \sin(\varphi/2) & \cos(\varphi/2) \end{pmatrix}, \tag{1.23}$$

where $\hat{I}$ is the identity matrix. Hence a null rotation (by $\varphi = 0$) is the identity, as expected. A rotation by $\varphi = \pi$ about the y axis is given by $R_y(\pi) = \begin{pmatrix} 0 & -1 \\ 1 & 0 \end{pmatrix}$, which will take the ground state $|g\rangle = (1, 0)$ to $|e\rangle = (0, 1)$, which is identified with the "south pole" of the Bloch sphere. A second rotation by π about y then yields the state $(-1, 0) = -|g\rangle$, i.e. rotating $|g\rangle$ by 2π about the y axis yields $-|g\rangle$. It takes a 4π rotation to take $|g\rangle$ back to itself, a well-known result for two-level systems. These rotations thus change the probabilities of the $|g\rangle$ and $|e\rangle$ states, by changing the angle θ in Eqn. (1.22). A similar outcome is achieved by rotations about the x axis, using σ_x. By contrast, rotations about the z axis keep the probabilities of the $|g\rangle$ and $|e\rangle$ states the same, but changes the relative phase ϕ in Eqn. (1.22).

Experimental quantum manipulations of the state of a phase qubit rely on the physics of the Josephson junction. Rotations about the z axis of the Bloch sphere are generated by waiting: The energy difference between these states results in different evolution rates for their phases, as dictated by the Schrödinger equation, Eqn. (1.15). The evolution rate can be varied by changing this energy difference, accomplished by adjusting the qubit bias s using the external flux bias applied to a flux bias coil patterned near the qubit; this changes the plasma frequency ω_p (Eqn. (1.16)) and thus the energy level spacing $\hbar\omega_q$. These changes in bias are quasi-static (i.e. not microwave signals, although the bias pulses sometimes only last a few tens of nanoseconds), so these are called dc pulses.

Rotations about the x and y axes represent changes in the relative populations of $|g\rangle$ and $|e\rangle$, and are generated experimentally by microwave tones set to the frequency ω_q of the ground and excited states: Rotations about x are achieved by applying tones set to the cosine quadrature of the phase of the microwave clock signal, while those about y are offset by 90°, using the sine quadrature. The tones are pulsed with Gaussian envelopes in time, carefully designed to minimize unwanted occupation of the higher qubit energy level $|f\rangle$, with amplitude and duration calibrated to give the desired outcome on the Bloch sphere.

1.2.2 Qubit readout

An important requirement of any quantum experiment is the ability to measure the outcome of the experiment. At a minimum, this requires that the experimentalist can distinguish between the final states $|g\rangle$ and $|e\rangle$. This is accomplished using a two-stage process in the phase qubit, performing first a projection of the phase qubit state, followed by a readout of the projection result.

In the projection stage, a pulse a few tens of nanoseconds in length is applied to the flux bias line to the qubit, changing the qubit energy splitting and more importantly tilting the qubit potential so that the barrier separating the left local minimum from the right absolute minimum is reduced. The $|e\rangle$ state, which sits at a higher energy and hence sees a smaller (lower and narrower) barrier than the $|g\rangle$ state, will tunnel out of the qubit well into the right well. When this occurs, the qubit is placed in a high quantum number state in that well, and the energy dissipation processes discussed above take over, causing the qubit to relax rapidly to the lowest few states in the right well (the rapid relaxation due to the high quantum number). This rapid relaxation

corresponds to the qubit emitting a significant amount of energy, and this process makes it unlikely that any quantum coherence remains in the qubit after this event; we assume that this process projects the qubit onto the right-hand well ground state when it was initially in the excited state in the left well, while it remains in the left well if it was initially in the ground state. This projection process thus forces an initial superposition of the ground and excited states into one outcome or the other, with probability determined by the squared amplitudes of the initial state. However, at this point the result of this projection is still not known.

The second stage in the measurement process is the readout of the projection outcome. This is accomplished by using the fact that the phase coordinate differs by close to 2π, depending on which of the two wells the qubit ends up in; this difference in phase corresponds to an overall change of flux in the qubit flux loop of one flux quantum Φ_0 (see e.g. Barone and Paterno 1982). This relatively large flux difference is easily measured by turning on a superconducting quantum interference device (SQUID) that is patterned next to, and closely coupled to, the qubit. The SQUID yields a different readout voltage depending on which of the two possible outcomes occurred, and this signal is digitized and recorded. This thus constitutes a read-out of the prior projection. This read-out and the subsequent relaxation and resetting of the qubit state takes about 100 μs to complete.

The process of projection and readout is performed once at the end of each experimental qubit sequence. The process destroys the qubit state, so any quantum information in the circuit is destroyed by the time the measurement is completed. The preparation protocol must then be repeated to acquire statistical information and to allow variation of the quantum experiment. In order to obtain a value for the qubit state probabilities, the measurement process is typically repeated several hundred to a few thousand times. The fraction of times the measurement outcome yields the excited state allows us to establish the excited state probability P_e; the probability that it was instead in the ground state is $P_g = 1 - P_e$. We can measure the excited state probability with a fidelity of about 95%, where the fidelity is limited by "false positives" in which the qubit in the ground state tunnels and the measurement reports an excited state, or "false negatives" where the qubit is in the excited state and fails to tunnel.

A series of measurements of a qubit only yields the state probabilities P_e and P_g; these tell us nothing about the relative phase ϕ of the $|g\rangle$ and $|e\rangle$ states. Phase information is obtained extending the measurement procedure in a process we term "quantum state tomography". In the first additional set of measurements, once the quantum experiment is complete, prior to projecting and reading out, we apply a microwave pulse that causes a Bloch sphere rotation about the x axis by $\varphi = \pi/2$; this microwave pulse is immediately followed by a standard measurement, which when repeated yields the probability that the x-rotated state is in the $|e\rangle$ state. The second additional set of measurements uses instead a rotation about the y axis by $\pi/2$, followed by measurement. The combination of these three sets of measurements yields the complex amplitudes that make up the state vector $|\psi\rangle$, i.e. it yields the angles θ and ϕ in Eqn. (1.22) (Steffen *et al.*, 2006). A full tomographic measurement involving ~ 3000 measurements takes about 3 seconds. In many experiments, we are interested in how the state vector $|\psi\rangle$ evolves as the qubit experimental parameters are varied, for

example by varying the qubit tuning, or a microwave pulse frequency or amplitude. In that case, a full tomographic measurement is carried out for each set of experimental parameters, with each parameter varied in turn to generate a map of qubit responses.

1.2.3 Qubit lifetime and phase coherence time

Two important parameters for a qubit are its energy lifetime (known as the T_1 time) and its phase coherence time (known as the T_ϕ time). The energy lifetime is determined by the amount of dissipation in the qubit circuit, as discussed above. The dissipation is measured in the quantum limit by preparing the qubit in its excited state $|e\rangle$, using a π microwave pulse to excite from $|g\rangle$ to $|e\rangle$, and then measuring the qubit state as a function of delay time after preparation. The qubit excited state probability P_e decays exponentially, with a characteristic lifetime T_1: $P_e = \exp(-t/T_1)$. The T_1 is related to the effective circuit quality factor Q and linear circuit parameters R and C by $T_1 = Q/\omega_q \approx RC$. By fitting the measured data to this form, we find the qubit lifetime. For the UCSB phase qubits, at present we typically find $T_1 \sim 600$ ns, with individual samples ranging from 400 to 900 ns. The effective resistance is then $R \sim 0.5$ MΩ.

The phase coherence time is the length of time a superposed state of the type $|\psi\rangle = |g\rangle + e^{i\phi}|e\rangle$ maintains a well-defined value for the phase ϕ (we ignore the normalization). Now, because of the difference in the qubit's energy levels, the excited state naturally evolves in time at the qubit frequency, i.e. the state will evolve according to $|\psi(t)\rangle = |g\rangle + e^{i\phi}e^{i\omega_q t}|e\rangle$. In order to measure the evolution of the phase ϕ, the much more rapid time dependence is taken out by using a microwave signal as a "clock" for the qubit. The measurement to extract T_ϕ is called a Ramsey fringe experiment. A microwave $\pi/2$ pulse about the y axis takes the ground state qubit to the $|g\rangle + |e\rangle$ state, and this state evolves in time. After a delay a second $\pi/2$ microwave pulse about y is used to "complete" the initial rotation, with the microwave frequency tuned to the qubit frequency ω_q, and the qubit state is then measured. Unfortunately, very slight de-tunings of the microwave frequency will mask the evolution of the qubit itself. A better measurement is therefore a spin-echo measurement: A π pulse about the x axis is applied at the midpoint of the wait time between the two y-axis $\pi/2$ pulses, and the resulting reversal of the qubit state about the equator acts to cancel out any error in the microwave frequency. The probability of measuring the qubit in its excited state typically decays according to a Gaussian $P_e = \exp(-(t/T_2)^2)$, both in phase qubits as well as charge qubits (Yoshihara *et al.*, 2006). This yields the T_2 time, which is related to the phase coherence time T_ϕ by $1/T_2 = 1/2T_1 + 1/T_\phi$, accounting for the decay of the excited state due to energy relaxation.

1.3 Harmonic oscillators

The phase qubit is a remarkable device in that its characteristic electrical impedance $1/\omega_q C \sim 30$ Ω, close to the characteristic impedance of 50 Ω used for most microwave components. This makes it easy to couple the phase qubit to other circuit elements. Furthermore, the self-capacitance of the phase qubit, about 1 pF, means that it can be connected to relatively long wires without overloading the qubit with stray capacitance. As a result, we have been able to simply couple the phase qubit to other

systems, allowing us to use the control and measurement technology we have developed for the phase qubit to probe and control other systems. Here we describe how we have been able to achieve complete quantum control over electromagnetic resonators. As discussed below, an electromagnetic resonator is a physical implementation of an idealized system, the harmonic oscillator; as such, these measurements reveal the quantum mechanical behavior of a harmonic oscillator.

Controlling and observing a harmonic oscillator in the quantum limit imposes certain challenges on the experimentalist. It is most interesting to work with a oscillator that is in its quantum ground state. Achieving the ground state requires reducing the thermal energy $k_B T$ to well below the energy level spacing $\hbar\omega_r$ of an oscillator with resonance frequency ω_r. If the experimentalist uses a commercial dilution refrigerator, with a base temperature of about 20 mK, it would be reasonable to ask that the energy level spacing be about 100 mK in temperature units – in other words, $\omega_r/2\pi$ should be greater than 2 GHz. However, even with the oscillator in the quantum ground state, achieving quantum control and quantum measurement capability is very hard if the experimentalist wishes to couple directly to the oscillator. We instead chose to control and measure a qubit, and to couple the qubit to the oscillator, whereby the coupled system allows for complete quantum control and measurement of the oscillator. This is best achieved if the oscillator and qubit can be brought into frequency resonance, as will be made clear below. We therefore designed our electromagnetic oscillators to have resonance frequencies $\omega_r/2\pi$ of around 6 GHz. When refrigerated to 20 mK, the probability of thermally-occupying the first excited state in such an oscillator is about $P_1 \approx \exp(-\hbar\omega_r/k_B T) \sim 10^{-5}$; the oscillator is thus safely in the quantum ground state.

In order to couple an oscillator to a qubit, however, the oscillator must interact with the voltages or currents generated in the qubit electrical circuit. The oscillator must also be compatible with the qubit fabrication; for example, it is easiest if the oscillator can be fabricated on the same physical chip, and at the same time, as the qubit. The oscillator must also have characteristics that allow strong coupling of the qubit and the oscillator; the coupling strength determines how long it takes for the qubit and oscillator to exchange energy, and if this time is too long compared to say the excitation lifetime in the qubit or the oscillator, it limits the degree of control that can be achieved. These requirements of course place severe constraints on what physical oscillator implementations can be explored. We have been able to achieve appropriate co-fabricated, strongly coupled systems with electromagnetic resonators, where the integration is relatively straightforward, as well as with piezoelectric mechanical resonators. Here we discuss the work with electromagnetic resonators, and refer the reader to other publications for details relating to the mechanical resonator experiments (Marquardt *et al.*, 2011; OConnell *et al.*, 2010).

1.3.1 Electromagnetic resonators

Electromagnetic resonators are structures that typically support multiple resonant modes at well-defined, and well-separated frequencies. There is a wide range of different possible geometries, including curved mirrors for free-space electromagnetic modes, completely enclosed cavities, and planar structures more compatible with thin-film in-

tegrated circuitry. Depending on the design and the materials used, very low electromagnetic loss is possible, so that excitations in the resonators will be very long-lived. The quality factor is a useful measure of the loss in a resonator, proportional to the number of oscillations an excitation will exhibit before decaying away. Defined in the frequency domain, the quality factor $Q = \omega/\Delta\omega$, where ω is the resonance frequency and $\Delta\omega$ the width of the resonance (full width at half maximum in the power response of the resonance). Using mirrored structures, quality factors as high as 10^{10} have been achieved in a resonator operating near 50 GHz (Kuhr *et al.*, 2007).

We have chosen to use half-wave coplanar stripline resonators, shown in Fig. 1.5. These consist of three parallel, co-planar strips of superconducting metal (typically either aluminum or rhenium), with a center signal conductor placed in-between two ground-plane electrodes. The resonators are patterned on low-loss single-crystal sapphire substrates (O'Connell *et al.*, 2008; Wang *et al.*, 2009*b*). We design the structures so that the fundamental (lowest frequency) electromagnetic mode falls in the 6-8 GHz range, which translates to a resonator length of about 8-10 mm. In the fundamental mode, the voltage between the signal and ground electrodes is a maximum at the open-terminated ends of the resonator, while it passes through a node at the geometric center of the resonator. In order to reduce the overall geometric footprint, the resonator is typically designed in a serpentine geometry. We place grounding straps at intervals along the length of the resonator, reaching from one ground electrode to the other, to better maintain a good ground at microwave frequencies. The straps pass over the signal electrode with an intervening insulating layer to prevent shorts; the insulating layer often dominates the loss in the structure.

The electromagnetic loss in these resonators is somewhat power-dependent, the power dependence becoming more marked in devices that include substantial quantities of amorphous dielectric; this is thought to be due to the presence of two-level fluctuators in poorer-quality dielectrics (Gao *et al.*, 2007; O'Connell *et al.*, 2008; Wang *et al.*, 2009*b*). When characterizing the performance, we therefore always reduce the measurement power to a minimum, as close as possible to the single photon limit; low-power quality factors of a few times 10^5 are typical. A measurement of a typical superconducting resonator is shown in Fig. 1.4. The finite Q of a resonator translates to a finite lifetime for an excitation in the resonator. This is quantified by the T_1 just as for a qubit, where the quality factor Q and energy lifetime T_1 are related by $T_1 = Q/\omega_r$ for a resonance frequency ω_r. A 6 GHz resonator with $Q = 10^5$ will have $T_1 = 2.6$ μs. Resonators also have phase coherence times, with a definition similar to that for a qubit; our resonators typically have pure phase coherence times of tens of microseconds (Wang *et al.*, 2009*b*).

A single mode in an electromagnetic resonator has an energy that can be calculated from the combined electric and magnetic fields that support the oscillation. The energy is quadratic in the field amplitude, and when written in quantized form using the photon raising and lowering operators, has exactly the form of a harmonic oscillator. We can therefore write the Hamiltonian for the resonator's fundamental mode as

$$\hat{H}_r = \left(\hat{a}^\dagger \hat{a} + \frac{1}{2}\right) \hbar\omega_r, \tag{1.24}$$

where $\hat{a}^\dagger$ is the photon raising (creation) operator, $\hat{a}$ the photon lowering (destruction)

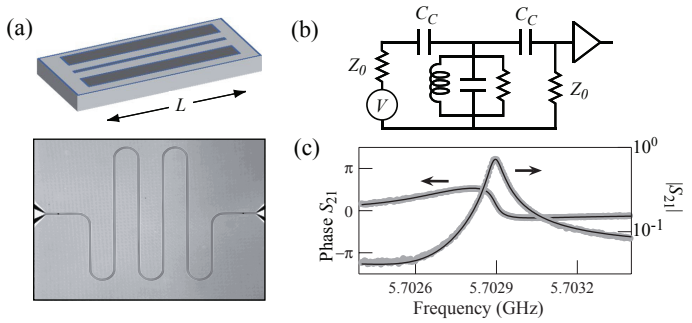

Fig. 1.4 (a) Upper: Schematic drawing of a half-wave coplanar stripline resonator, with three metal strips (dark) comprising two ground electrodes (outer) and an inner signal electrode. The length L of stripline is varied to select the resonance frequency. Lower: Image of stripline resonator, with undulations to reduce the footprint; triangular elements on left and right are bond pads for electrical connections. The resonator itself is terminated by small inline coupling capacitors along the length of the center strip (not visible). The micrograph horizontal dimension is just under 6 mm. (b) Equivalent circuit for the lowest frequency resonance, modeled as a parallel RLC circuit, with coupling capacitors C_c to the excitation (left) and detection (right) ports. The impedance Z_0 is the characteristic impedance of measurement circuit. (c) Transmitted phase of S_{21} (left scale) and magnitude (right scale) as a function of frequency, showing the characteristic resonant response. The resonance frequency is at 5.7029 GHz. Grey is data, solid black line is the fit. Adapted from A. D. O'Connell et al., *Appl. Phys. Lett.* **92**, 112903 (2008).

operator, and ω_r the resonator resonance frequency (in radians/second), all for the fundamental mode. See e.g. Haroche and Raimond 2006 for a discussion of the quantum harmonic oscillator.

1.4 Coupled qubit and resonator

We couple a qubit to an electromagnetic resonator using a lumped, in-line coupling capacitor, connected between the qubit and one end of the stripline resonator (where the voltage is a maximum); see Fig. 1.5. The coupling capacitor is chosen to balance the need for fast transfers that avoid significant state decay in either the qubit or the resonator, with the desire for slow transfers that improve the fidelity of quantum operations, which are otherwise limited by the speed of our control electronics. Some of the errors associated with the limited electronics speed can be corrected by using "overshoots" and other modifications of the tuning pulses (Motzoi *et al.*, 2009). We have found that a reasonable compromise for these competing needs is to use coupling capacitors that give transfer times of 20 to 50 ns, that is, transfer rates of 20-40 MHz, the slower rates compatible with qubits with longer T_1 and T_2 times (the qubit times tend to be much shorter than the corresponding resonator times).

As is explained below, we often need to inject classical microwave pulses into the resonator. We connect a microwave cable to the other end of the resonator from the

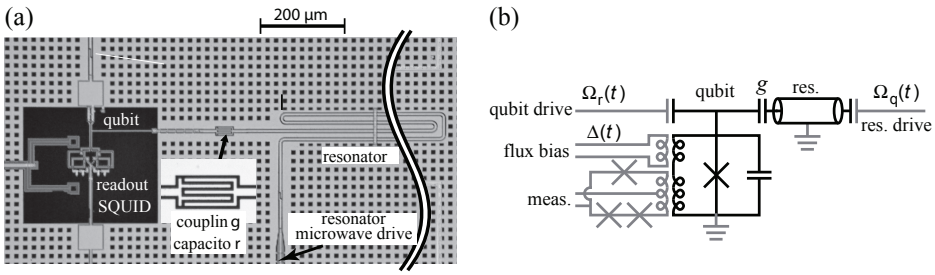

Fig. 1.5 (a) Micrograph of a phase qubit (left) coupled to a coplanar waveguide resonator (right). The resonator has a total length of 8.76 mm and resonance frequency of 6.56 GHz. A capacitor couples the qubit to the resonator, shown inset in the image. The resonator can also be directly excited using a second capacitively-coupled microwave line at the opposite end to the qubit, also shown inset in the image. (b) Qubit and resonator circuit. The qubit is in the center, the resonator on the right, and the control lines and measurement SQUID for the qubit on the left. Adapted from M. Hofheinz et al., *Nature* **454**, 310-314 (2008).

qubit using a second, much smaller coupling capacitor, to minimize the coupling of unwanted noise from the microwave cable into the resonator, as well as minimize the effect of the low-impedance cable on the resonator quality factor. We note that all the microwave cables on our dilution refrigerator are very heavily filtered above about 20 GHz, and all those not transmitting microwave signals filtered above about 500 MHz. The microwave lines have typically 40 dB of attenuation over all frequencies, with a 20 dB attenuator at the mixing chamber temperature to minimize the coupling of thermal noise into the qubit circuit. Many experimental details can be found in Markus Ansmann's and Matthew Neeley's PhD theses (Ansmann, 2009; Neeley, 2010).

An image of a completed resonator and qubit is shown in Fig. 1.5. Once a device has been fabricated and tested at room temperature, it is mounted in an aluminum microwave mount, with electrical connections made with aluminum wire bonds. The mount is placed on the mixing chamber plate of our dilution refrigerator, microwave cable connections are made, and the refrigerator cooled to about 25 mK (the device is in vacuum). We first perform functional tests of the qubit and its readout SQUID, and then test the resonator by making a spectroscopic measurement.

A qubit spectroscopy measurement is begun by applying a short (few tens of nanoseconds), weak microwave pulse to the microwave line connected to the qubit (using the flux coil used to bias the qubit), and the qubit excited state probability P_e then measured. This is repeated for different microwave frequencies ω and qubit frequencies ω_q, the latter controlled by varying the dc flux bias on the qubit bias line. The microwave excitations are small enough that the qubit excited state probability is at most 30-50%. The measured response is shown in Fig. 1.6, where the qubit and microwave frequencies are tracked together to measure the resonant response. The qubit frequency varies as expected, with the microwave excitation generating a measurable change in P_e when the microwave frequency $\omega/2\pi$ (vertical axis) matches the qubit frequency $\omega_q/2\pi$, as determined by the bias (horizontal axis). When the qubit frequency

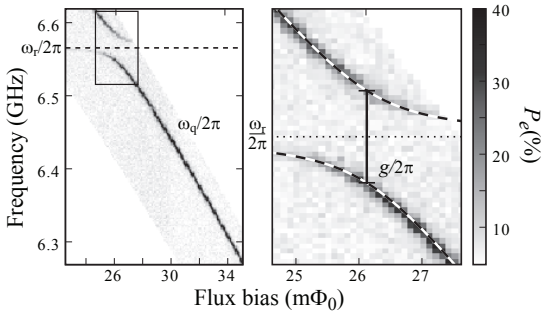

Fig. 1.6 Qubit spectroscopy. False gray-scale image shows excited state probability P_e of the qubit as a function of microwave frequency and flux bias in units of the flux quantum $\Phi_0 = h/2e$. A dark line is seen when the frequency of the microwave drive matches an eigenfrequency of the coupled qubit-resonator system. An avoided crossing appears when the qubit is tuned through the resonator frequency. A detailed view of the avoided crossing is shown on the right, superposed with a fit to the interaction Hamiltonian (dashed black and white line). Adapted from M. Hofheinz et al., *Nature* **454**, 310-314 (2008).

ω_q approaches the resonator frequency ω_r, the qubit begins to interact strongly with the resonator, so the microwave pulse excites the combination of qubit and resonator. An avoided-level crossing therefore appears in the spectroscopy for ω_q near ω_r. The detailed response can be fit exactly, using the resonator frequency and qubit-resonator coupling strength as fit parameters.

The spectroscopic response of the coupled qubit and resonator can be understood using classical physics: Two coupled harmonic oscillators, one of which is tuned by varying say its mass, will have natural *classical* eigenmodes, as a function of the tuned mass, that reproduce closely the behavior seen in Fig. 1.6. The quantum behavior appears when one considers the relation between the excitation amplitude (as measured by P_e) and the microwave excitation energy. This we explore below; understanding this however requires a quantum description of the coupled system.

When the qubit is strongly de-tuned from the resonator, no energy is exchanged between the two, due to the very weak transfer at large de-tuning. By contrast, when the qubit is placed exactly into resonance with the resonator, energy is exchanged rapidly between the two systems, and the system oscillates. The quantum dynamics of this interaction can be approximated within the rotating-wave approximation by the Jaynes-Cummings model interaction Hamiltonian (Jaynes and Cummings, 1963; Neeley, 2010),

$$\hat{H}_{\text{int}} = \frac{\hbar g}{2}\left(\hat{a}\hat{\sigma}_+ + \hat{a}^\dagger\hat{\sigma}_-\right), \tag{1.25}$$

where $\hat{a}^\dagger$ and $\hat{a}$ are the photon creation and annihilation operators for the resonator, and σ_+ and σ_- the qubit raising and lowering operators, as discussed above. The coupling strength $g/2\pi$ is determined by the qubit-resonator coupling capacitor, and can be measured from the spectroscopic response (Neeley *et al.*, 2008): The difference in frequency of the points of closest approach in the avoided level crossing in Fig. 1.6 is

equal to $2(g/2\pi)$. We note that this description applies to the case where there is only a fraction (less than one) photon in the circuit; more complex behavior is observed when multiple photons are injected (see e.g. Dykman and Ivanov 1976; Schuster *et al.* 2005).

The full Hamiltonian in the rotating-wave approximation can be written as

$$\begin{aligned}\hat{H} &= \hbar\Delta(t)\hat{\sigma}_+\hat{\sigma}_- + \frac{\hbar g}{2}\left(\hat{a}\hat{\sigma}_+ + \hat{a}^\dagger\hat{\sigma}_-\right) \\ &+ \frac{\hbar}{2}\left(\Omega_{\rm q}(t)\hat{\sigma}_+ + \Omega_{\rm q}^\star(t)\hat{\sigma}_-\right) + \frac{\hbar}{2}\left(\Omega_{\rm r}(t)\hat{a}^\dagger + \Omega_{\rm r}^\star(t)\hat{a}\right).\end{aligned} \tag{1.26}$$

The first term is the qubit energy, where $\Delta(t) = \omega_q(t) - \omega_r$ is the (time-dependent) qubit de-tuning from the resonator, where the time dependence is achieved through the external flux bias control of the qubit energy. The second term is the interaction with the resonator, and the third and fourth terms account for external microwave excitation of the qubit and resonator, with $\Omega_q(t)$ and $\Omega_r(t)$ the time-dependent, complex-valued microwave amplitudes for the qubit and resonator, respectively. Note that the resonator energy appearing in Eqn. (1.24) has dropped out of the full Hamiltonian due to the rotating-wave transformation (Carmichael, 2007; Neeley, 2010).

Although the qubit-resonator coupling g is fixed, we control the qubit-resonator interaction by adjusting the qubit frequency $\Delta(t)$, where $\Delta = 0$ corresponds to the qubit and resonator in resonance; we call this the on-resonance point, $\Delta_{\rm on} = 0$. We effectively turn off the interaction by switching the qubit to $|\Delta_{\rm off}| \approx 25g$.

To inject one photon into the resonator, we first allow the qubit tuned to $\Delta_{\rm off}$ to relax to its ground state, by waiting about 100 μs. With the resonator also in its ground state $|n = 0\rangle$, the system is in the combined state $|g\rangle|0\rangle$. We then excite the qubit to the $|e\rangle$ state using an on-resonance, calibrated microwave pulse $\Omega_q(t)$ that rotates the qubit about the Bloch sphere y axis by π. This results in the state $|\psi\rangle = |e\rangle|0\rangle$. This state can be achieved with greater than 95% fidelity (Lucero, Hofheinz, Ansmann, Bialczak, Katz, Neeley, O'Connell, Wang, Cleland and Martinis, 2008). We then bring the qubit and resonator into exact resonance ($\Delta_{\rm on} = 0$), so that the coupling term involving g in the Hamiltonian begins to transfer the single excitation between the qubit and the resonator. By waiting, the system will alternate between the $|e\rangle|0\rangle$ state and the state where the qubit is in its ground state with one photon in the resonator, $|\psi\rangle = |g\rangle|1\rangle$. This oscillation occurs at the one-photon "Rabi-swap" frequency g, as can be seen from the interaction term in the Hamiltonian (1.26). Note that when the same process is performed, but with a non-zero de-tuning $\Delta \neq \Delta_{\rm on}$, the system oscillates between the same two states $|e\rangle|0\rangle$ and $|g\rangle|1\rangle$, but at a higher frequency $\sqrt{g^2 + \Delta^2}$, and with reduced probability for the $|g\rangle|0\rangle$ state, $P_{g0} = g^2/(g^2 + \Delta^2) < 1$.

This process is shown in Fig. 1.7 for a small range of de-tunings $-g \lesssim \Delta \lesssim g$. The agreement with the model described above is extremely good. The on-resonance tuning point, with $\Delta = 0$, and the interaction time needed to achieve a high fidelity transfer swap from $|e\rangle|0\rangle$ to $|g\rangle|1\rangle$, $\tau = 28$ ns in Fig. 1.7, is calibrated using this measurement. We note that at our typical off-resonance operating point $\Delta_{\rm off} \approx -25g$ (far off the limits of the data shown in the figure), the photon transfer probability is only 0.0016, so the coupling is indeed effectively turned off.

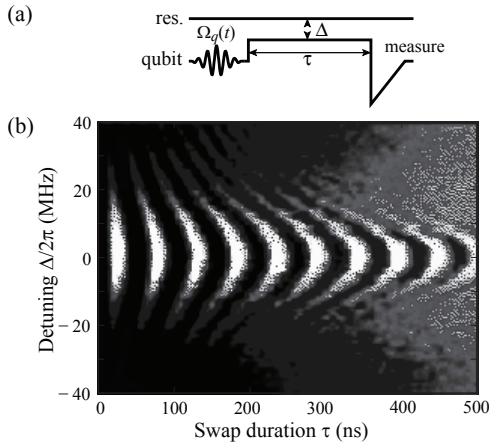

Fig. 1.7 (a) Pulse sequence to excite qubit and then perform one-photon Rabi swaps with the resonator; after a microwave pulse excitation $\Omega_q(t)$, the qubit is tuned to within Δ of the resonator frequency, and the qubit excited state probability P_e then measured. This sequence is performed as a function of interaction time τ. (b) Measured one-photon Rabi swaps, showing the expected oscillation in time τ, with the correct dependence on time and de-tuning Δ (vertical axis). The excited state probability P_e is indicated by the color scale on the left. Adapted from M. Hofheinz et al., *Nature* **459**, 546-549 (2009).

1.4.1 Preparation of photon Fock states

We can now apply the Rabi swap process we have just described to generate photon Fock states (number states) in the resonator. We can generate a $n = 1$ photon Fock state by stopping the Rabi swap interaction just described at the minimum in the excited state probability in Fig. 1.7, i.e. at $\tau = 28$ ns $= \pi/g$ with zero de-tuning $\Delta_{\rm on} = 0$. We turn off the interaction at that point by de-tuning the qubit from the resonator to $\Delta_{\rm off}$. The resonator is then left in the Fock state $|n = 1\rangle$, with the qubit in its ground state $|g\rangle$. Following this, more photons can be placed in the resonator by repeating the sequence: The qubit is excited to $|e\rangle$, tuned to resonance $\Delta_{\rm on}$, the excitation swapped to the resonator, and the qubit de-tuned to $\Delta_{\rm off}$. This protocol is illustrated in Fig. 1.8. Each repetition transfers one more photon into the resonator, until the desired photon number is reached, yielding the desired final state $|g\rangle|n\rangle$. We note that for the nth excitation, the term $\hat{a}^\dagger\hat{\sigma}_-$ in the Hamiltonian Eqn. (1.26), operating on the state $|e\rangle|(n-1)\rangle$, yields the state $\sqrt{n}|g\rangle|n\rangle$, so the swap rate increases with excitation number n as $\sqrt{n}$. Equivalently, the system Rabi oscillates between the state $|g\rangle|n\rangle$ and the state $|e\rangle|n-1\rangle$ at the Rabi frequency $\sqrt{n}\,g$. To account for this, the nth photon swap time is shortened from the one-photon swap time by the factor $1/\sqrt{n}$. This $\sqrt{n}$ dependence of the Rabi frequency is equivalent to the process of stimulated emission in a laser: A photon is transferred between resonator and qubit more rapidly when more photons are present in the system. This dependence of the Rabi frequency on excitation number n is the key to how analyzing the final resonator state (Brune

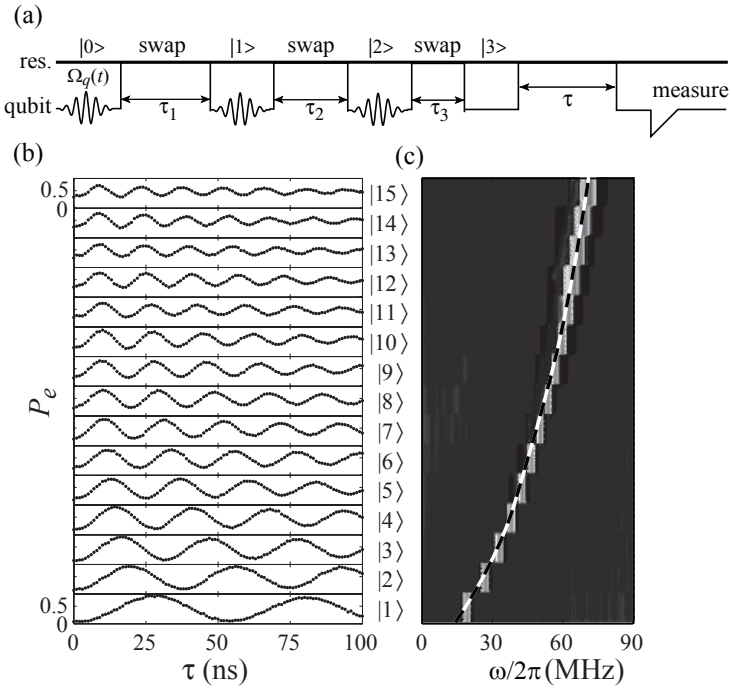

Fig. 1.8 (a) Microwave pulse and qubit tuning sequence to generate a $n = 3$ Fock state in the resonator. The last step is to interact the initially ground state qubit with the resonator for an interaction time τ and then measure the qubit state. (b) Probability of the qubit excited state P_e versus interaction time τ for resonator Fock states from $n = 1$ to $n = 15$. The time traces show the expected sinusoidal dependence with a period that shortens with increasing photon number n. (d) Fourier amplitude of the traces in (c). Each Fourier transform has a peak at the n-photon oscillation frequency $\sqrt{n}\, g/2\pi$, indicating the high purity of the Fock states. Dashed line is the expected scaling using the coupling strength $g/2\pi = 19$ MHz. Adapted from M. Hofheinz et al., *Nature* **454**, 310-314 (2008).

et al., 1996).

1.4.2 Measurement of a Fock state

To measure the resonator state at the end of the preparation process, we tune the ground state qubit into resonance with the resonator, and leave it there for a time τ before measuring the qubit state. The measured probability $P_e(\tau)$ is shown in Fig. 1.8(c). The probability is expected to evolve according to (Haroche and Raimond, 2006)

$$P_e(\tau) = \sum_{n=1}^{\infty} P_n \, \frac{1 - \cos(\sqrt{n} g \tau)}{2}, \tag{1.27}$$

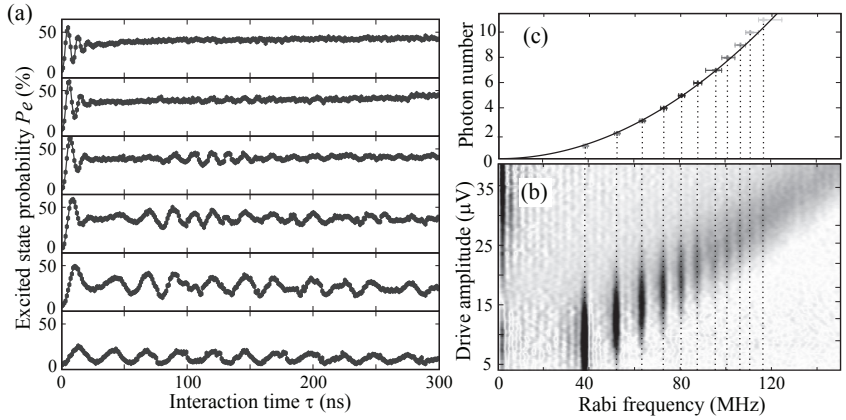

Fig. 1.9 (a) Coherent state analysis. Excited-state probability P_e versus interaction time τ for coherent states generated with a range of microwave amplitudes. (b) Fourier transform of the data in (a). Darker colors indicate higher Fourier amplitudes. The Fourier spectrum reveals a sharp maximum at each number-state frequency, from $n = 1$ to 11 photons. (c) Frequencies of the number state Fourier peaks compared to the expected $\sqrt{n}$ scaling. Adapted from M. Hofheinz et al., *Nature* **454**, 310-314 (2008).

where P_n is the probability to have n photons in the resonator. For a pure Fock state $|n\rangle$, P_e should oscillate between 0 and 1, with oscillation frequency $\sqrt{n}g/2\pi$. For a superposition of Fock states, the time dependence of $P_e(\tau)$ is more complicated. The zero-photon probability P_0 does not enter Eq. (1.27), but is instead calculated from the time average

$$\overline{P_e} = \sum_{n=1}^{\infty} P_n/2 = (1 - P_0)/2. \tag{1.28}$$

The time traces in Fig. 1.8(c) are closely sinusoidal, indicating that for each initial resonator state, one photon number n dominates in the response. The oscillations have large amplitude, decreasing in time τ due to energy decay, and also gradually decreasing with increasing n. Both the amplitude of the oscillations in P_e, and the decay time decrease with n. This is as expected, as the lifetime of an n-photon Fock state decreases as T_r/n (Schwinger, 1961; Lu, 1989); the decrease in initial amplitude with n seen in the figure is due to the time needed to prepare the nth state increases with n, so the state has already decayed somewhat prior to the beginning of the measurement sequence. A more complete analysis of this dependence is shown in Fig. 1.8d, where the Fourier transforms of the time traces are plotted: Each transform displays a clear peak at a single frequency, the frequency given by $\sqrt{n}g/2\pi$. The white line superposed on the data shows the expected $\sqrt{n}$ scaling.

1.4.3 Coherent states in the resonator

We can use a classical microwave source to inject a classical energy pulse into the resonator, and then use the qubit to analyze the outcome. The expectation is that for

a smooth pulse, the resonator state should closely match that of a coherent state, the quantum equivalent of a classical oscillation. In order to generate such a state, we use a Gaussian-shaped microwave pulse set to the resonator frequency, with a full-width at half maximum envelope of 100 ns (see Fig. 1.9b). Different amplitude coherent states are generated by varying the amplitude of the microwave pulse. The qubit, de-tuned from the resonator, remains in its ground state during this process. We then measure the resonator using the qubit, exactly as was done for the analysis of the Fock states.

In a coherent state, the amplitude and phase of the excitation in the resonator are well-defined, but the number of photons is not. We can nonetheless de-convolve a coherent state into its composition in terms of the Fock states $|n\rangle$. A coherent state will have an occupation probability P_n for the nth Fock state given by the Poisson distribution,

$$P_n = \frac{\bar{n}^n}{n!} e^{-\bar{n}}, \tag{1.29}$$

where $\bar{n}$ is the average number of photons in the coherent state. When the qubit is brought into resonance with a resonator in such a state, each of the Fock states will interact with the qubit. The resulting qubit response is a superposition of the Rabi oscillations associated with each photon number n, each with its own (irrational) swap frequency $\sqrt{n}\, g$. The measured response, for a range of different microwave amplitudes, i.e. a range of coherent states with different average photon numbers $\bar{n}$, is shown in Fig. 1.9(a). The figure shows the qubit excited state probability P_e as a function of interaction time with the coherent-state resonator. At low drive amplitudes, where $\bar{n} < 1$ (on average less than one photon in the resonator), the qubit excited-state probability oscillates in a periodic fashion, but with low visibility due to the small occupation of the resonator $|1\rangle$ state, and even smaller occupation of the number states above $|1\rangle$. At higher drive amplitudes, with larger $\bar{n}$, the probability displays a strong initial onset with a rapid collapse, followed by a revival, a characteristic feature for a coherent state coupled to a two-level system (Faist *et al.*, 1972; Eberly *et al.*, 1980). During the revival part, the irregular time dependence is due to the irrational relative frequencies of the different Fock number states.

The behavior of the excited state probability is more easily understood by examining the Fourier transform of the time traces, shown in Fig. 1.9(b). The oscillation frequency associated with the state $|n\rangle$ appears as a sharp vertical line, with amplitude determined by the probability P_n that the state participates in the coherent state, as given by Eqn. (1.29). The spectrum provides strong validation of the underlying quantum nature of the coherent states. As the drive amplitude increases, the signal due to higher photon numbers become more pronounced, and there is significant occupation for a wider range of photon numbers. In Fig. 1.9(c), the oscillation frequencies corresponding to the maxima of these lines are plotted versus photon number, and match those observed for the pure Fock states.

The amplitudes of the probability data in Fig. 1.9(a) show good quantitative agreement with the expected Poisson distribution, and the dependence of photon number on drive amplitude also agrees well with that expected; see Hofheinz *et al.* 2009. This provides very strong evidence that our microwave Gaussian pulses generate coherent

states in the resonator, which gives us an important tool for performing resonator quantum state tomography, as described below.

1.4.4 Arbitrary photon states in a resonator

With the successful generation of Fock states, the next goal was to directly synthesize arbitrary superpositions of these states. As before, the qubit is used to generate the states, and the same qubit serves to measure the result. We would like to generate a general resonator state $|\psi\rangle$, with the qubit in its ground state:

$$|\psi\rangle = |g\rangle \otimes \sum_{n=0}^{N} c_n |n\rangle, \tag{1.30}$$

with complex amplitude c_n for the nth Fock state. It was shown by Law and Eberly (Law and Eberly, 1996) that such states can be generated by a sequence of excitations of the qubit followed by state transfers from the qubit to the resonator. The excitation of the qubit however is typically a partial one, leaving the qubit in a mixture of its ground and excited states, rather than a full Rabi swap from $|g\rangle$ to $|e\rangle$ as was used in the Fock state generation. A sequence that generates a particular desired state can be found by solving the time-reversed problem: Starting with the desired final state, we first transfer the amplitude of the highest occupied resonator photon number state to the qubit, and then remove that excitation from the qubit by de-tuning the qubit from the resonator and using a classical microwave signal to swap the qubit to its ground state. This completely deterministic process is then repeated until the system ground state $|g\rangle|0\rangle$ is reached. The actual generation of the final state is accomplished by time-reversing this sequence, taking the system from the initial ground state to the desired final state. We correct the relative phases of $|g\rangle|n\rangle$ and $|e\rangle|n-1\rangle$, an important adjustment needed to get a specific final state, by adjusting the time t_n during which the qubit is de-tuned from the resonator.

Details regarding the microwave preparation pulses, the calibrations, and the sequences worked out to generate specific final states are documented in Hofheinz *et al.* 2009. A basic check of any preparation sequence is done by measuring if the qubit ends up in its ground state $|g\rangle$ at the end of the pulse sequence, as desired. We found that this always occurred with a probability greater than 80%, the remaining 20% compatible with the expected qubit decoherence occurring during the preparation sequence. With the qubit demonstrably in its ground state (thus not entangled with the resonator), we can then use the qubit to measure the resonator state. We bring the qubit into resonance with the resonator for a time τ, and measure the excited state probability P_e as a function of this interaction time. From this measurement we determine, as described above for the Fock state analysis, the n-photon probabilities $P_n = |c_n|^2$. However this measurement does not allow us to measure the phases of the amplitudes c_n.

To completely measure the complex amplitudes c_n, we therefore need a more complete measurement technique. This is provided by Wigner tomography (Banaszek and Wödkiewicz, 1996; Banaszek *et al.*, 1999; Haroche and Raimond, 2006), which gives the Wigner quasi-probability distribution $W(\alpha)$ of the resonator. Here α is the coordinate

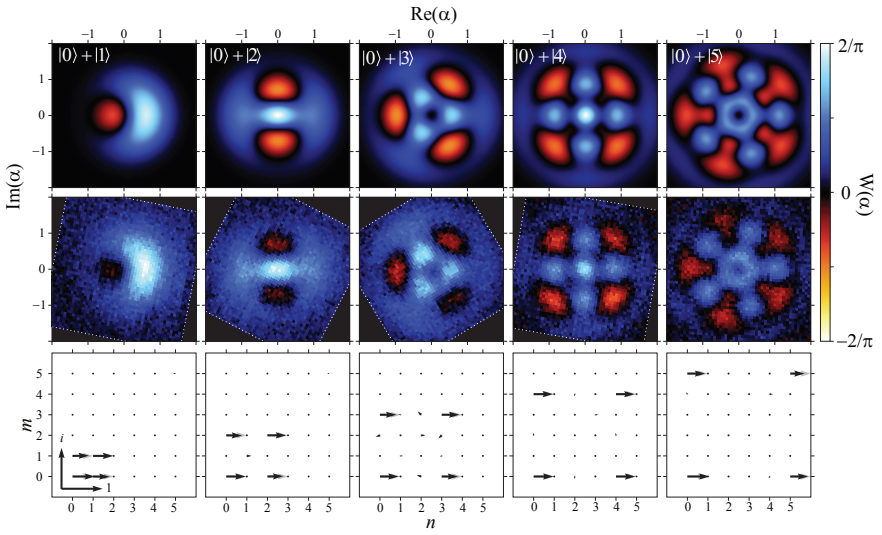

Fig. 1.10 (Color) Wigner tomography of the superposition states $|0\rangle + |n\rangle$. The top row displays the calculated form for the Wigner function $W(\alpha)$ as a function of the resonator amplitude α (in square-root-of-photon-number units), for the states $(|0\rangle + |n\rangle)/\sqrt{2}$, with n from 1 to 5. The measured Wigner tomograms are shown in the second row, with the color scale bar on the right. Each of the ~ 2500 pixels in each of the measured Wigner tomograms represents the accumulation of about 3000 measurments. Negative quasi-probabilities are clearly measured. The experimental Wigner tomograms have been rotated to match the orientation of the calculated functions, compensating for time delays in the control microwave lines. The third row displays the calculated (grey) and measured (black) density matrices ρ, in the number state basis $\rho_{mn} = \langle m|\hat{\rho}|n\rangle$. The magnitude and phase of each element is represented by the length and direction of an arrow in the complex plane (see scale bottom left). This direct mapping of a Wigner tomogram takes $\sim 10^8$ measurements or about five hours. Adapted from M. Hofheinz et al., *Nature* **459**, 546-549 (2009).

of a point in the complex resonator phase space (where amplitude corresponds to the square root of photon number and angle to the microwave phase). Wigner tomography is performed by implementing the functional definition

$$W(\alpha) = \frac{2}{\pi}\langle\psi|D^{\dagger}(-\alpha)\,\Pi\,D(-\alpha)|\psi\rangle, \tag{1.31}$$

where $D(-\alpha)$ is a displacement operator that displaces the resonator state by $-\alpha$ in its phase space, and Π is the resonator parity operator. The displacement $D(-\alpha)$ is achieved experimentally by injecting a Gaussian microwave drive pulse $-\alpha = (1/2)\int \Omega_r(t)\mathrm{d}t$ into the resonator, prior to measuring $P_e(\tau)$. The photon number probabilities P_n are then extracted from $P_e(\tau)$ in the usual way, and the parity $\langle\Pi\rangle = \sum_n (-1)^n P_n$ is directly evaluated from the measured probabilities. This then yields the value of the Wigner function for that value of α (once multiplied by $2/\pi$ as

in Eq. (1.31)). The value of α is then swept over an appropriate range of microwave amplitudes and phases, generating a direct map of the Wigner function.

In Fig. 1.10 we compare the calculated and measured Wigner functions for the resonator states $(|0\rangle+|n\rangle)/\sqrt{2}$, with $n = 1$ to 5. The functions match quite well, including fine details, illustrating that both the state synthesis and the Wigner tomography are being performed with good fidelity. The density matrices can be calculated from the Wigner tomograms (see Hofheinz *et al.* 2009) and are in good agreement with expectations. The direct mapping of the Wigner function we show here is an important verification of our state preparation.

The comparisons in Fig. 1.10 do not prove control over the relative phase of the two superposed Fock states, as changes in the phase of one of the two states only rotates the Wigner tomogram, just as would occur for a change e.g. in the microwave cable lengths. We can demonstrate phase control by instead superposing three appropriately-chosen Fock states; changing one of the superposed states' phase will change the actual form, rather than the orientation, of the Wigner tomogram. Figure 4 in Hofheinz *et al.* 2009 shows the results for the synthesis and measurement of the states $|\psi\rangle = (|0\rangle + e^{i\phi}|3\rangle + |6\rangle)/\sqrt{3}$, where the phase ϕ is changed in each of the series of panels in the figure (not reproduced here). The good agreement between the calculated and measured Wigner functions indicates good phase control in the state synthesis. The calculated and measured density matrices also match well.

We can also build more complex superpositions states, as is shown in Fig. 1.11, where we display the "voodoo cat" state, which involves Fock states up to $n = 9$. The state shown there is a superposition of synthetic approximations to three coherent states. First, we have the coherent state $|\alpha_1\rangle$ with $\bar{n} = 4$ (amplitude of 2) and zero phase; second the state $|\alpha_2\rangle$ with the same number of photons (amplitude 2) but a phase of 120°, and finally the state $|\alpha_3\rangle$ with the same number of photons but a rotation of 240°. By expressing each of these states in the number state basis, and adding up the terms with the same photon numbers, you can show that the superposed state can be written as

$$|\psi\rangle = \sum_{n=0,3,6\ldots} \frac{2^n}{\sqrt{n!}} |n\rangle. \tag{1.32}$$

In order to generate this state synthetically, we truncated the sum at $n = 9$ photons, where the difference between the full sum and the synthetic result is nearly indistinguishable due to the rapidly decreasing amplitude with n.

The measured and calculated Wigner tomograms, shown in Fig. 1.11, agree quite well, as do the calculated and measured density matrices. This demonstrates we can synthetically generate states with up to $n = 9$ photons with good amplitude and phase control.

In conclusion, we can confidently state that we have demonstrated excellent quantum control as well as measurement of a simple harmonic oscillator, in the form of one electromagnetic mode of a coplanar stripline resonator. The high quality factor (long T_1) of the resonator is one of the keys to achieving such good control, as is the excellent control we have over the Josephson phase qubit that was used to control and to measure the oscillator. Future experiments will continue to explore the happy

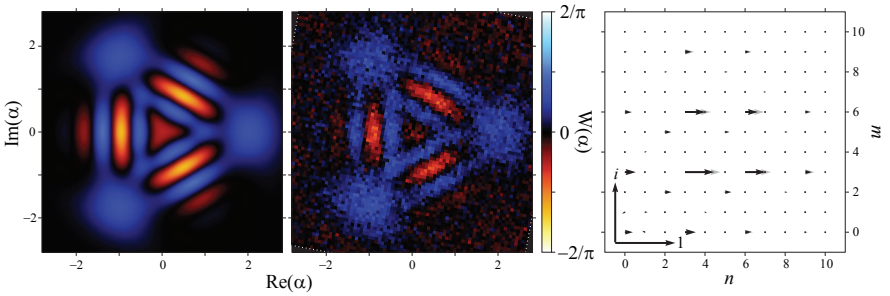

Fig. 1.11 (Color) Figure shows the calculated (left) and measured (center) Wigner tomograms for a "voodoo cat" state. The right panel is the comparison of the density matrices, as for the $|0\rangle + |n\rangle$ states. The state shown here is an equal superposition of coherent states $|\alpha_1 = 2\rangle$ ("alive"), $|\alpha_2 = 2e^{2\pi i/3}\rangle$ ("dead") and $|\alpha_3 = 2e^{4\pi i/3}\rangle$ ("zombie"). Theory and experiment are seen to match quite well, with a calculated fidelity of 0.9, indicating that states up to nine photons can be accurately synthesized.

marriage of these two elements. We have succeeded in establishing quantum entanglement of two physically-separated resonators, placed on the same chip but about a millimeter apart. Entanglement allowed us to demonstrate the direct synthesis of microwave-photon NOON states, with N photons in one resonator and zero in the other, superposed with the state with zero photons in the first resonator and N in the second (Wang *et al.*, 2011). These states were verified by simple coincidence measurements, where detecting N photons in one resonator is always correlated with zero photons detected in the other, as well as complete, bipartite Wigner tomography of the entangled resonators. This tomography reveals strong off-diagonal elements in the density matrix, validating that entanglement has been achieved. We have also built more complex circuits, in which for example we are able to play "hide-and-seek" with photons in three microwave resonators, and demonstrate a quantum version of the confidence trick known as the "shell game" (Mariantoni *et al.*, 2011).

The precise quantum control and measurements we have demonstrated with a microwave-frequency electromagnetic resonator, as outlined in this chapter, has thus laid the groundwork for new modalities of quantum control as well as a new form for a quantum computer architecture.

References

Ansmann, M. A. (2009). *Benchmarking the Superconducting Josephson Phase Qubit: The Violation of Bell's Inequality.* Ph.D. thesis, University of California - Santa Barbara.

Banaszek, K., Radzewicz, C., Wódkiewicz, K., and Krasiński, J. S. (1999). Direct measurement of the Wigner function by photon counting. *Phys. Rev. A*, **60**, 674–677.

Banaszek, K. and Wödkiewicz, K. (1996). Direct probing of quantum phase space by photon counting. *Phys. Rev. Lett.*, **76**, 4344–4347.

Barone, A. and Paterno, G. (1982). *Physics and Applications of the Josephson Effect.* Wiley, New York.

Benz, S. P. and Hamilton, C. A. (1996). A pulse-driven programmable Josephson voltage standard. *Appl. Phys. Lett.*, **68**, 3171–3173.

Brune, M., Schmidt-Kaler, F., Maali, A., Dreyer, J., Hagley, E., Raimond, J. M., and Haroche, S. (1996). Quantum Rabi oscillation: A direct test of field quantization in a cavity. *Phys. Rev. Lett.*, **76**, 1800–1803.

Caldeira, A. O and Legget, A (1981). Influence of dissipation on quantum tunneling in macroscopic systems. *Phys. Rev. Lett.*, **46**, 211.

Carmichael, H. J. (2007). *Statistical Methods in Quantum Optics.* Springer.

Chiorescu, I., Bertet, P., Semba, K., Nakamura, Y., Harmans, C. J. P. M., and Mooij, J. E. (2004). Coherent dynamics of a flux qubit coupled to a harmonic oscillator. *Nature*, **431**, 159–162.

Chiorescu, I., Nakamura, Y., Harmans, C. J. P. M., and Mooij, J. E. (2003). Coherent quantum dynamics of a superconducting flux qubit. *Science*, **299**, 1869–1871.

Clarke, J., Cleland, A. N., Devoret, M. H., Esteve, D., and Martinis, J. M. (1988). Quantum mechanics of a macroscopic variable: the phase difference of a Josephson junction. *Science*, **239**, 992–997.

Cooper, K. B., Steffen, Matthias, McDermott, R., Simmonds, R. W., Oh, Seongshik, Hite, D. A., Pappas, D. P., and Martinis, John M. (2004). Observation of quantum oscillations between a josephson phase qubit and a microscopic resonator using fast readout. *Phys. Rev. Lett.*, **93**, 180401.

Devoret, M. H, Martinis, J. M, and Clarke, J (1985). Measurements of macroscopic quantum tunneling out of the zero-voltage state of a current-biased josephson junction. *Phys. Rev. Lett.*, **55**, 1908.

Dykman, M. I. and Ivanov, M. A. (1976). Spectral distribution of resonant localised impurity vibrations at finite temperatures. *Sov. Phys. Solid State*, **18**, 415–420.

Eberly, J. H., Narozhny, N. B., and Sanchez-Mondragon, J. J. (1980). Periodic spontaneous collapse and revival in a simple quantum model. *Phys. Rev. Lett.*, **44**, 1323–1326.

Faist, A., Geneux, E., Meystre, P., and Quattropani, P. (1972). Coherent radiation in interaction with two-level system. *Helv. Phys. Acta*, **45**, 956.

Gao, J., Zmuidzinas, J., Mazin, B. A., LeDuc, H. G., and Day, P. K. (2007). Noise properties of superconducting coplanar waveguide microwave resonators. *Appl. Phys. Lett.*, **90**, 102507.

Geller, M. R. and Cleland, A. N. (2005). Superconducting qubits coupled to nano-electromechanical resonators: An architecture for solid-state quantum-information processing. *Phys. Rev. A*, **71**, 032311.

Goldstein, Herbert, Poole, Charles, and Safko, John (2002). *Classical Mechanics*. Addison Wesley.

Haroche, S. and Raimond, J.-M. (2006). *Exploring the Quantum: Atoms, Cavities and Photons*. Oxford University Press, Oxford UK.

Hofheinz, M., Wang, H., Ansmann, M., Bialczak, R. C., Lucero, E., Neeley, M.and O'Connell, A. D., Sank, D., Wenner, J., Martinis, J. M., and Cleland, A. N. (2009). Synthesising arbitrary quantum states in a superconducting resonator. *Nature*, **459**, 546–549.

Hofheinz, M., Weig, E. M., Ansmann, M., Bialczak, R. C., Lucero, E., Neeley, M., O'Connell, A. D., Wang, H., Martinis, J. M., and Cleland, A. N. (2008). Generation of Fock states in a superconducting quantum circuit. *Nature*, **454**, 310–314.

Jaynes, E.T. and Cummings, F.W. (1963). Comparison of quantum and semiclassical radiation theories with application to the beam maser. *Proc. IEEE*, **51**, 89–109.

Josephson, B. D. (1962). Possible new effects in superconducting tunnelling. *Phys. Lett.*, **1**, 251.

Kuhr, S., Gleyzes, S., Guerlin, C., Bernu, J., Hoff, U. B., Delglise, S., Osnaghi, S., Brune, M., Raimond, J .M., Haroche, S., Jacques, E., Bosland, P., and Visentin, B. (2007). Ultrahigh finesse Fabry-Prot superconducting resonator. *Appl. Phys. Lett.*, **90**, 164101.

Law, C. K. and Eberly, J. H. (1996). Arbitrary control of a quantum electromagnetic field. *Phys. Rev. Lett.*, **76**, 1055–1058.

Leggett, A. J., Chakravarty, S., Dorsey, A. T., Fisher, Matthew P. A., Garg, Anupam, and Zwerger, W. (1987). Dynamics of the dissipative two-state system. *Rev. Mod. Phys.*, **59**, 1–85.

Lehnert, K. W., Bladh, K., Spietz, L. F., Gunnarsson, D., Schuster, D. I., Delsing, P., and Schoelkopf, R. J. (2003). Measurement of the excited-state lifetime of a microelectronic circuit. *Phys. Rev. Lett.*, **90**, 027002.

Lu, N. (1989). Effects of dissipation on photon statistics and the lifetime of a pure number state. *Phys. Rev. A*, **40**, 1707–1708.

Lucero, E., Hofheinz, M., Ansmann, M., Bialczak, R. C., Katz, N., Neeley, M., O'Connell, A. D., Wang, H., Cleland, A. N., and Martinis, J. M. (2008). High-fidelity gates in a single josephson qubit. *Phys. Rev. Lett.*, **100**, 247001.

Mariantoni, M., Wang, H., Bialczak, R. C., Lenander, M., Lucero, E., Neeley, M., O'Connell, A. D., Sank, D., Weides, M., Wenner, J., Yamamoto, T., Yin, Y., Zhao, J., Martinis, J. M., and Cleland, A. N. (2011). Photon shell game in three-resonator circuit quantum electrodynamics. *Nature Physics*, **7**, 287–293.

Marquardt, F., Aspelmeyer, M., and Kippenberg, T. (2011). *Optomechanics*, Chapter

Microwave-frequency mechanical resonators operated in the quantum limit. Springer (to be pubhlished).

Martinis, John M., Nam, S., Aumentado, J., and Urbina, C. (2002). Rabi oscillations in a large josephson-junction qubit. *Phys. Rev. Lett.*, **89**, 117901.

Mooij, J. E., Orlando, T. P., Levitov, L., Tian, Lin, van der Wal, Caspar H., and Lloyd, Seth (1999). Josephson persistent-current qubit. *Science*, **285**, 1036–1039.

Motzoi, F., Gambetta, J. M., Rebentrost, P., and Wilhelm, F. K. (2009). Simple pulses for elimination of leakage in weakly nonlinear qubits. *Phys. Rev. Lett.*, **103**(11), 110501.

Neeley, M. (2010). *Generation of Three-Qubit Entanglement Using Josephson Phase Qubits*. Ph.D. thesis, University of California - Santa Barbara.

Neeley, M., Ansmann, M., Bialczak, R. C., Hofheinz, M., Katz, N., Lucero, E., O'Connell, A. D., Wang, H., Cleland, A. N., and Martinis, J. M. (2008). Process tomography of quantum memory in a josephson-phase qubit coupled to a two-level state. *Nature Physics*, **4**, 523–526.

O'Connell, A. D., Ansmann, M., Bialczak, R. C., Hofheinz, M., Katz, N., Lucero, E., McKenney, C., Neeley, M., Wang, H., Weig, E. M., Cleland, A. N., and Martinis, J. M. (2008). Microwave dielectric loss at single photon energies and millikelvin temperatures. *Appl. Phys. Lett.*, **92**, 112903.

OConnell, A. D., Hofheinz, M., Ansmann, M., Bialczak, R. C., Lenander, M., Lucero, E., Neeley, M., Sank, D., Wang, H., Weides, M., Wenner, J., Martinis, J. M., and Cleland, A. N. (2010). Quantum ground state and single-phonon control of a mechanical resonator. *Nature*, **464**, 697–703.

Pashkin, Yu. A, Yamamoto, T, Astafiev, O, Nakamura, Y, Averin, D. V, and Tsai, J. S (2003). Quantum oscillations in two coupled charge qubits. *Nature*, **421**, 823–826.

Sakurai, J. J. and Napolitano, J. (2011). *Modern quantum mechanics* (2nd edn). Addison Wesley.

Schuster, D. I., Wallraff, A., Blais, A., Frunzio, L., Huang, R.-S., Majer, J., Girvin, S. M., and Schoelkopf, R. J. (2005). ac Stark shift and dephasing of a superconducting qubit strongly coupled to a cavity field. *Phys. Rev. Lett.*, **94**, 123602.

Schwinger, J. (1961). Brownian motion of a quantum oscillator. *J. Math. Phys.*, **2**, 407–432.

Simmonds, R. W., Lang, K. M., Hite, D. A., Nam, S., Pappas, D. P., and Martinis, John M. (2004). Decoherence in josephson phase qubits from junction resonators. *Phys. Rev. Lett.*, **93**, 077003.

Steffen, M., Ansmann, M., McDermott, R., Katz, N., Bialczak, R. C., Lucero, E., Neeley, M., Weig, E. M., Cleland, A. N., and Martinis, J. M. (2006). State tomography of capacitively shunted phase qubits with high fidelity. *Phys. Rev. Lett.*, **97**, 050502.

Tinkham, M. (2004). *Introduction to Superconductivity* (2 edn). Dover Publications.

van der Wal, Caspar H., ter Haar, A. C. J., Wilhelm, F. K., Schouten, R. N., Harmans, C. J. P. M., Orlando, T. P., Lloyd, Seth, and Mooij, J. E. (2000). Quantum superposition of macroscopic persistent-current states. *Science*, **290**, 773–777.

Wallraff, A., Schuster, D. I., Blais, A., Frunzio, L., Huang, R.-S., Majer, J., Kumar,

S., Girvin, S. M., and Schoelkopf, R. J. (2004). Strong coupling of a single photon to a superconducting qubit using circuit quantum electrodynamics. *Nature*, **431**, 162–167.

Wang, H., Hofheinz, M., Ansmann, M., Bialczak, R.C., Lucero, E., Neeley, M., OConnell, A. D., Sank, D., Wenner, J., Cleland, A. N., and Martinis, J. M. (2008). Measurement of the decay of fock states in a superconducting quantum circuit. *Phys. Rev. Lett.*, **101**, 240401.

Wang, H., Hofheinz, M., Ansmann, M., Bialczak, R. C., Lucero, E., Neeley, M., O'Connell, A. D., Sank, D., Weides, M., Wenner, J., Cleland, A. N., and Martinis, J. M. (2009*a*). Decoherence dynamics of complex photon states in a superconducting circuit. *Phys. Rev. Lett.*, **103**, 200404.

Wang, H., Hofheinz, M., Wenner, J., Ansmann, M., Bialczak, R. C., Lenander, M., Lucero, E., Neeley, M., O'Connell, A. D., Sank, D., Weides, M., Cleland, A. N., and Martinis, J. M. (2009*b*). Improving the coherence time of superconducting coplanar resonators. *Appl. Phys. Lett.*, **95**, 233508.

Wang, H., Mariantoni, M., Bialczak, R. C., Lenander, M., Lucero, E., Neeley, M., OConnell, A. D., Sank, D., Weides, M., Wenner, J., Yamamoto, T., Yin, Y., Zhao, J., and Cleland, J M. Martinisand A. N. (2011). Deterministic entanglement of photons in two superconducting microwave resonators. *Phys. Rev. Lett.*, **106**, 060401.

Yamamoto, T, Pashkin, Yu. A, Astafiev, O, Nakamura, Y, and Tsai, J. S (2003). Demonstration of conditional gate operation using superconducting charge qubits. *Nature*, **425**, 941.

Yoshihara, F., Harrabi, K., Niskanen, A. O., Nakamura, Y., and Tsai, J. S. (2006). Decoherence of flux qubits due to $1/f$ flux noise. *Phys. Rev. Lett.*, **97**, 167001.

Index

Bloch sphere, 8

Coplanar stripline resonator, 13

Energy lifetime T_1, 11

Jaynes-Cummings Hamiltonian, 16
Josephson junction, 1
  Charging energy E_c, 4
  Josephson energy E_J, 4
  Josephson frequency, 3
  Josephson relations, 2
  phase difference δ, 2
  phase qubit, 6
  tunnel junction, 2

Law and Eberly protocol, 22

Pauli matrices, 7, 8
Phase coherence time T_ϕ, 11
Phase qubit, 6
Photon states
  arbitrary, 22
  coherent, 21
  Fock, 18
  raising and lowering operators, 13
  Voodoo, 24

Qubit spectroscopy, 15

Wigner function, 22
Wigner tomography, 22